SwissFEL double bunch operation

Martin Paraliev,[*] Arturo Alarcon, Vladimir Arsov, Simona Bettoni, Roger Biffiger, Marco Boll, Hans Braun, Alessandro Citterio, Paolo Craievich, Andreas Josef Dax, Philipp Dijkstal, Sladana Dordevic, Eugenio Ferrari,[†] Franziska Frei,[‡] Romain Ganter, Zheqiao Geng, Christopher Gough, Nicole Hiller, Martin Huppert, Rasmus Ischebeck, Pavle Juranic, Mario Jurcevic, Babak Kalantari, Roger Kalt, Boris Keil, Christoph Kittel, Waldemar Koprek, Daniel Llorente, Florian Löhl, Alexander Malyzhenkov,[§] Fabio Marcellini, Goran Marinkovic, Gian Luca Orlandi, Cigdem Ozkan Loch, Marco Pedrozzi, Eduard Prat, Sven Reiche, Colette Rosenberg, Thomas Schietinger, Serguei Sidorov, Alexandre Trisorio, Carlo Vicario, Didier Voulot, Guanglei Wang, and Riccardo Zennaro

Paul Scherrer Institute, 5232 Villigen, Switzerland

(Received 7 July 2022; accepted 4 November 2022; published 2 December 2022)

SwissFEL has a unique capability, among the normal conducting linac-based light sources, to simultaneously serve two separate undulator lines (Aramis and Athos) up to the machine repetition rate of 100 Hz using the double bunch operation mode. It increases twice the experiments throughput of the facility with modest additional investment. Two electron bunches spaced 28 ns apart are extracted from the cathode by two laser pulses with individually controlled repetition rates. The bunches are accelerated up to about 3 GeV in the main linac using the same rf macropulse. After separation, one bunch serves the Athos soft x-ray beamline and the other is further accelerated to serve the hard x-ray beamline – Aramis. A fast and high-stability beam kicker separates the two bunches without disturbing the electron beam and consequently the x-ray lasing. The timing and control system sets hybrid machine modes utilizing independent operation of the two undulator lines with individually programmed repetition rates. Beam diagnostics and feedback systems have to operate with two closely spaced bunches where the two beams share the same machine path. The low-level rf system manipulates the rf amplitude and phase within a fraction of the rf macropulse to provide decoupling of the acceleration parameters of the first and the second bunch. This manuscript presents measurements that show that the bunch separation does not degrade FEL lasing stability.

DOI: 10.1103/PhysRevAccelBeams.25.120701

I. INTRODUCTION

SwissFEL is a linac-based x-ray free-electron laser (FEL) user facility at the Paul Scherrer Institute in Switzerland [1]. It is capable of producing FEL radiation with pulse energies at the millijoule level, pulse durations of a few tens of femtoseconds, and relative bandwidths between one and few per mil, providing photon beams for experimental research in material science, biophysics, biochemistry, and other fields. It has a hard x-ray (Aramis) and soft x-ray (Athos) undulator line covering wavelength ranges from 0.1 to 0.6 nm (12.4–2.0 keV) and 0.65 to 5.0 nm (1.9 to 0.25 keV) respectively [2–4]. Both lines can operate simultaneously and independently up to the maximum machine repetition rate (100 Hz) providing x-ray pulses to several (two at a time) experimental stations.

Thanks to the SwissFEL double bunch operation, the two experimental lines are decoupled and can provide individually chosen wavelengths, pulse durations, and repetition rates.

II. MOTIVATION AND SCOPE

Linac-based x-ray sources have important advantages compared to synchrotron-based ones, like much higher pulse energies and shorter pulse duration, but due to their straight-line topology, operating multiple undulator lines from the same electron beam is a challenge. This, together with the fact that these are single-pass machines,

[*]martin.paraliev@psi.ch

[†]Present address: Deutsches Elektronen-Synchrotron, Notkestraße 85, 22607 Hamburg, Germany.

[‡]Present address: Federal Institute of Metrology, 3003 Berne-Wabern, Switzerland.

[§]Present address: CERN, Esplanade des Particule 1, 1211 Geneva, Switzerland.

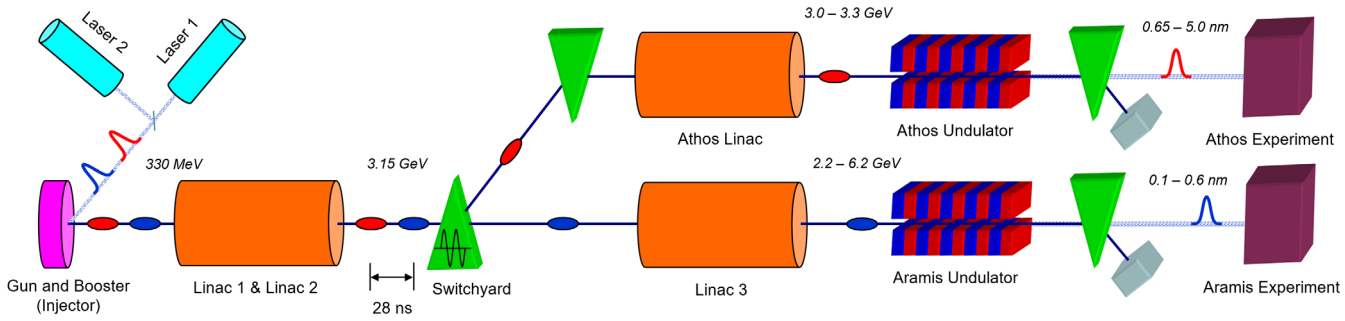

FIG. 1. SwissFEL layout.

substantially increases the cost per experimental station with respect to the synchrotron-based ones.

Different schemes (like static or dynamic beam distribution [5,6] and beam sharing [7]) are used to increase the efficiency of such facilities. Beam distribution systems are used to send electron bunches to different undulator lines statically (serving one beamline at a time) or dynamically (continuously distributing bunches to several beamlines). The dynamic distribution uses fast deflecting elements (kickers) to route bunches to their respective beamlines in order to serve them quasi-simultaneously. A drawback of this method is that if more than one line is served, they operate at a reduced repetition rate and accordingly receive reduced total photon flux.

In beam-sharing schemes, bunches pass through two (or more) undulators sequentially and are used to produce light simultaneously. The main drawback of the scheme is that after each undulator, the beam quality degrades (due to induced energy spread by the FEL process) and the following undulators cannot benefit from the full machine capabilities. This usually limits the number of simultaneously used undulators to two and constrains the operation of the second one. Without additional effort, the repetition rate of the consecutive beamlines is the same (or lower than the one in the previous undulator) and the pulse length is the same due to the usage of the same electron bunch [8].

On the other hand, a couple of FELs have demonstrated two-bunch operation (mainly) targeting pump-and-probe experiments, exploring the possibilities to accelerate bunches with ns temporal separation in the same normal conducting linac but lasing in the same photon beamline [9,10].

SwissFEL is taking a unique approach in order to ensure simultaneous and decoupled operation of its two undulator lines up to the maximum machine repetition rate despite its normal conducting linacs. Two electron bunches spaced 28 ns apart are accelerated in the same rf macropulse to up to 3.15 GeV and then separated and sent to their respective beamlines (Fig. 1). The bunch dedicated to the hard x-ray line is further accelerated up to 6.2 GeV (Linac 3) providing the necessary additional beam energy. Both undulator lines can receive bunches with individually set energy, charge, and repetition rate depending on user needs. Independent undulator and bunch compression settings, in combination with additional acceleration or deceleration, allow for different x-ray pulse lengths, energies, polarizations, and wavelengths in each experimental station. Decoupled machine protection reduces unnecessary downtime due to problems in the not relevant machine sections.

Although the doubled throughput makes it more cost-effective, the double bunch operation has a large impact on several accelerator systems. The requirement for efficient and (almost) equal acceleration of the two-electron bunches in one rf macropulse hinges on close temporal bunch spacing. On the other hand, too closely spaced bunches present a challenge to the separation kicker, low-level rf (LLRF) system, and beam diagnostics. Moreover, the long-range wakes excited by the first bunch may degrade the second bunch [11].

The nonharmonic frequencies for S-band injector (2.9988 GHz) and C-band main linac (5.7120 GHz) of SwissFEL set an additional timing limitation that a synchronous bunch can be accelerated only every 7 ns [12].

A bunch separation of 28 ns was chosen as an engineering compromise between the technological capabilities and limitations of all affected accelerator systems.

We will discuss in more detail the specific systems and technical solutions necessary to realize double bunch operation at SwissFEL.

III. PHOTOCATHODE DRIVE LASERS FOR TWO-BUNCH GENERATION

The first key subsystems are the PhotoCathode Drive Lasers (PCDLs) that must deliver two, 3.3–10 ps FWHM, deep-UV pulses ($\lambda = 260$ nm) separated by exactly 28 ns to generate the two electron bunches. The pulse duration, energy, and temporal shape must be independently adjustable. Figure 2 shows the 3D optical setup in detail.

The laser system also has to provide two so-called laser heater (LH) pulses [13]. The arrival time of the PCDL pulses must be set and stabilized with femtosecond accuracy. These requirements are fulfilled by using two independent $Yb:CaF_2$ PCDL systems. We can see the two

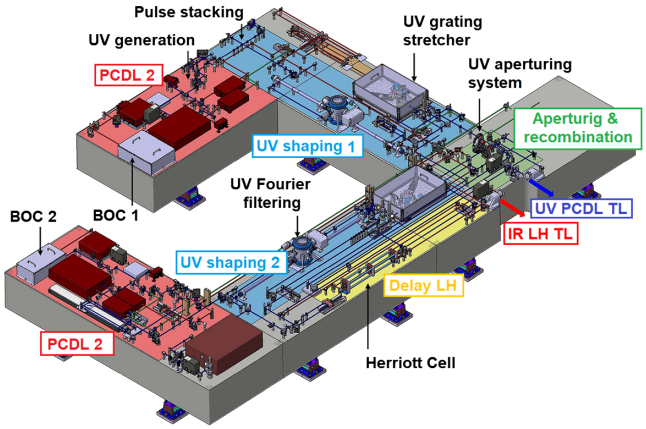

FIG. 2. 3D CAD layout of the SwissFEL dual-PCDL optical setup. The photocathode drive lasers 1 and 2 (red areas) deliver temporally and spatially shaped deep-UV pulses (blue areas and green area) as well as the LH and short "probe" pulses for the two FEL lines. The two UV-PCDL and the two LH beams are recombined, respectively (green area), and sent toward the accelerator through two dedicated imaging transfer lines. The yellow area includes the LH Herriott cell used to delay the two LH pulses.

laser systems: PCDL 1 and 2, as well as the balanced optical correlators, used to stabilize the amplified pulse arrival time (red areas in Fig. 2). A subsequent fourth harmonic generation stage provides the conversion to deep-UV wavelengths. Temporal shaping (using α-BBO pulse stacking or a UV grating stretcher) as well as spatial filtering (UV Fourier filtering) stages are also shown (blue areas). The two UV-PCDL pulses must be recombined and spatially shaped before being relayed to the accelerator through an in-vacuum imaging transfer line (green area). The two LH pulses are similarly recombined and relayed down to the accelerator section. The correct arrival time of the bunch extraction pulses on the photocathode and LH pulses at the LH for all operation modes is challenging and required a careful design of the optical paths and automatic delay compensation using motorized delay stages and a Herriott cell optical setup (yellow area). The dual amplifier architecture increases the system's flexibility and reliability with regard to FEL operation. A detailed overview of the SwissFEL dual PCDL architecture, capabilities, and performance can be found in the literature [14,15].

IV. INDIVIDUAL ACCELERATION CONTROL

A. Acceleration

The double bunch operation illustrated in Fig. 1 imposes strict requirements on the SwissFEL LLRF system. It has to enable the acceleration of the two closely spaced bunches in the same rf macropulse with independently tunable accelerating voltage and phase. Therefore, the LLRF system should provide the following functions: a. Equalize the accelerating voltage and phase for the two bunches such that both bunches can be successfully transmitted through the machine. b. Tune the accelerating voltage and phase for the second bunch without disturbing the first bunch.

The latter function is important for independent acceleration parameters adjustment in parallel operation and was very helpful for Athos beamline commissioning simultaneously with user operation in Aramis.

The SwissFEL rf system consists of different types of accelerating structures: S-band standing-wave (SW) cavity for the rf gun, S-band/X-band traveling-wave (TW) structures for the injector, and C-band TW structures for the linacs [16]. For the double bunch operation, we are particularly interested in the rf stations in the common part of the two bunches upstream of the second bunch compressor.

A simple way to implement the above-described function "a" is to produce a flat rf pulse in both amplitude and phase [17]. However, to implement function "b," we need a knob to change the accelerating voltage and phase experienced by the second bunch. In principle, if function "b" is implemented and has sufficient tuning range, function "a" is automatically achieved as well.

LLRF typically manipulates the rf input to adjust the accelerating voltage and phase seen by the beam. Therefore, we tune the second bunch by introducing a step in the rf pulse using the LLRF system as shown in Fig. 3. An rf pulse step is applied after the first bunch such that it only affects the second one. Due to the 28 ns spacing of the two bunches, the maximum changes in the accelerating voltage and phase for the second bunch are determined by the step setting and the time constant of the SW cavity or the filling time of the TW structures. The rf pulse step is characterized by the step amplitude ratio (percentage of the original amplitude) and the step phase (phase shift with respect to the original phase).

The tuning ranges of the accelerating voltage and phase for the second bunch with amplitude step ratio between 0% and 100% and a step phase between −60° and 60° are summarized in Table I. The maximum amplitude step ratio is set to 100% to limit klystron peak power and to prevent

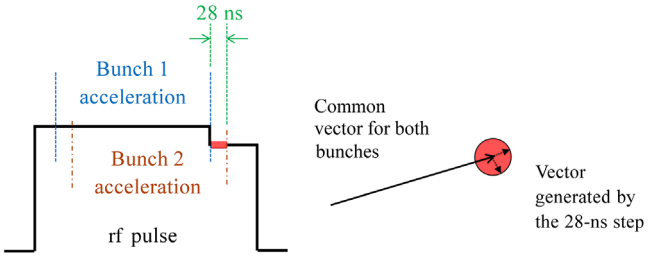

FIG. 3. LLRF strategy to tune the second bunch by introducing a step in the amplitude and the phase of the input rf pulse. The right plot is the vector representation of the method for the TW structures. The relevant region of the rf pulse for the first or for the second bunch acceleration corresponds to the filling time of the structures.

TABLE I. Second bunch tuning range.

rf station type	Frequency (GHz)	Filling time (ns)	Accelerating voltage range (%)	Accelerating phase range (°)
SW gun	2.9988	440	−1.8 to 0.9	±1.3°
S-band TW	2.9988	920	−1.7 to 0.0	±0.8°
C-band TW	5.7120	320	−4.8 to 2.9	±0.9°
X-band TW	11.9952	100	−21.6 to 0.0	±11.5°

breakdowns. The step phase range limits are chosen to ensure stable feedback operation.

The above scheme also works for the C-band stations equipped with rf pulse compressors (barrel open cavity type) with nonregular rectangular pulse shapes. Table I indicates that the rf pulse step tends to reduce the accelerating voltage. Therefore, before applying the step, we should optimize the rf pulse delay such that the second bunch receives more energy gain [18]. This helps to position the accelerating voltage tuning range symmetrically around zero (see Fig. 4 for an example).

The SwissFEL accelerator is typically optimized using the first bunch for successful beam transmission and desired beam parameters. Before switching on the second bunch for the first time, the rf pulse steps for all rf stations are pretuned so that both bunches receive similar accelerations, which is important for the successful transmission of the second bunch. We use the first bunch (already optimized) to pretune the rf pulse step. First, we determine the start time of the step within the rf pulse.

To do this, we shorten the rf pulse gradually (with a resolution of 4 ns defined by the LLRF clock cycle) and observe the first bunch energy. At some point, the energy begins to drop indicating the end of the rf pulse portion that affects the first bunch. The start of the step should be set after this point for the step to affect only the second bunch [19]. Then, we use the following procedure to pretune the rf pulse step using the first bunch: 1. After the first bunch is optimized, we save its parameters (energy, bunch length, arrival time, etc.). 2. We shift the timing of the first bunch to the time of the second bunch. 3. By adjusting the rf pulse step amplitude ratio and the phase step iteratively, we restore the beam parameters as saved in the first step. In this way, we equalize roughly the accelerating voltage and phase for both bunches.

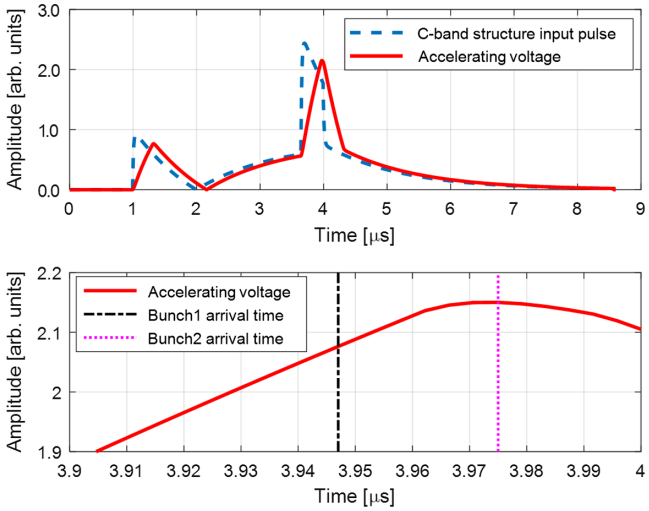

FIG. 4. Input pulse shape and energy gain in C-band stations (upper graph) and magnified energy gain slope and the position of the two bunches on it (lower graph). Note the different time scale for the two graphs.

Figure 5 shows the panel for rf gun pretuning. The bunch energy and the energy spread are measured using a spectrometer screen at the gun exit and are used as tuning criteria. When pretuning the rf pulse step, we only use one (the first) bunch. When both bunches are present, the second bunch will be affected by the presence of the first one due to beam loading in the rf structures, the Schottky effect in the rf gun, and long-range wakefields induced by the first bunch. The rf pulse step settings should be further optimized when the second bunch is successfully transmitted through the machine in the presence of the first one. Typically, we regulate the second bunch parameters using a separate feedback loop by actuating on the rf pulse step.

At present, dynamic compensation depending on the presence of the first bunch is not available and we cannot compensate dynamically the beam-loading effects created by the first bunch. This limits the available repetition rate configurations of the machine.

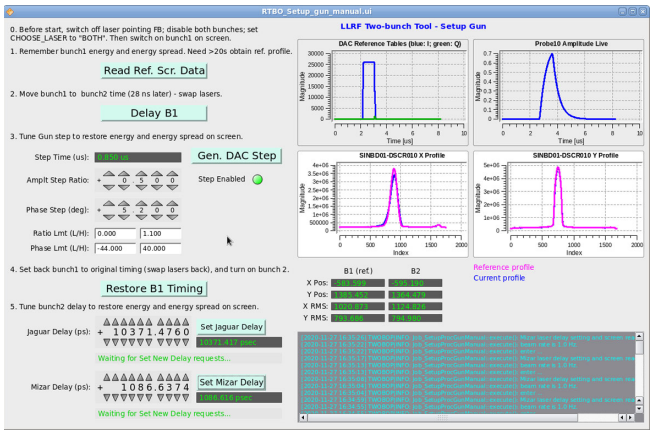

FIG. 5. Panel for rf pretuning.

B. Bunch compression

The SwissFEL two-bunch compression scheme is based on nearly identical compression settings for the two bunches, apart from small corrections for variations in charge and orbit, and differences due to user demands. The only free parameters to control the compression of each bunch independently are the rf settings since the longitudinal dispersion (R_{56}) of the bunch compressors is common to both bunches. The energy chirp can be adjusted for different compression but the mean energy should be identical for both bunches. This is necessary to avoid orbit steering due to the corrector quadrupoles, skew quadrupoles, and sextupoles in the bunch compressor lattice. In addition, an offset in the corrector sextupole due to energy deviation results in a small quadrupole component and thus adds a transverse tilt to the second bunch.

The quadrupole and sextupole magnets in the bunch compressors are primarily configured and optimized to remove any residual transverse tilt in the first bunch, which is driving the Aramis beamline. We assume that the corrections benefit the second bunch if both follow the same trajectory through the machine. Any small deviation in the beam orbit and tilt can still be corrected in the second bunch, once it is extracted into the Athos switchyard arm.

The switchyard was designed to provide a certain degree of R_{56} and thus some fine-tuning of the bunch length with the residual energy chirp of the second bunch, before it is removed by the dechirpers [20]. However, an increase in the septum separation and a shift in the mean energy at the switchyard make it impossible to achieve an isochronous configuration without extreme values for the Twiss function. Therefore, the switchyard was initially set up with an R_{56} of about 2 mm which slightly decompresses the bunch. This can be compensated by placing the second bunch more off-crest, thus compressing it slightly stronger than the first one. In practice, however, this causes very strong coherent synchrotron radiation (CSR) effects in the second bunch compressor and the Lambertson septum.

We recently, reconfigured the optics in the switchyard, abandoning the initial constraint of zero dispersion in the middle part of the switchyard in favor of a controlled R_{56}. The new design optics provides a slight compression of about $R_{56} = -1$ mm with still small optics function values all along the beamline. It enables lower compression in the second bunch compressor and thus reducing the impact of CSR significantly.

As mentioned earlier, the rf allows for different rf phases while preserving the mean energy at the bunch compressor. We typically have equivalent beam properties after BC1 (in the Booster) for both bunches, and we tune the pulse duration of the second bunch independently by adjusting its Linac 1 phase (C-band). Assuming that the first bunch stays at nominal conditions (200 pC charge with 25-fs rms duration), based on operational experience and consistent with the numbers given in Table I, the pulse duration of the second bunch can be changed by ± 50 fs rms by tuning the Linac-1 phase, where the negative duration values (for example in the above-mentioned case) will indicate an overcompression. Adjusting not only the Linac-1 phase but also the injector phases independently gives us a larger flexibility. In particular, the X-band is the preferred knob since it combines high sensitivity to compression and a larger tuning range of its phase. Including the injector knobs, the tuning range of the individual pulse duration is at least doubled with respect to tuning only by Linac 1. We recently demonstrated the operation of the first bunch in overcompression (with a large offset phase in Linac 1) while keeping the pulse duration of the second bunch as in standard operation (but with the penalty of having a larger energy chirp).

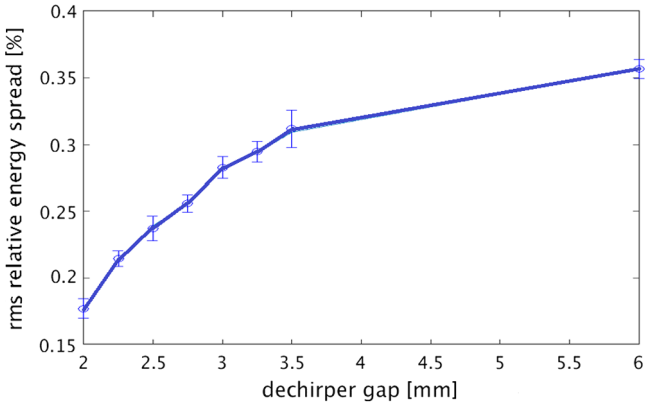

FIG. 6. Projected energy spread as a function of the gap of six dechirper modules.

This was possible by compressing less in the first bunch compressor to avoid overcompression in the second bunch compressor. A precise measurement of the full tuning range still needs to be done, in particular when operating both bunches at different charges. After the switchyard, the second bunch has a residual energy chirp of about 0.4% rms. For the first bunch, the chirp is normally removed with the wakefields of Linac 3. Eight corrugated structures in the Athos branch are planned to remove the chirp for the second bunch [21]. The efficiency of the dechirper in the soft x-ray line (Athos) has been measured with six modules installed (out of eight modules planned) and it is shown in Fig. 6. Down to a gap of 2 mm, a reduction in the projected energy spread in the beam dump screen is still noticeable, indicating that the chirp is not completely removed. One more dechirper module is to be installed soon. Afterward, the measurement will be repeated and cross-checked with the settings giving minimum SASE bandwidth in Athos.

V. TWO-BUNCH BEAM INSTRUMENTATION

Diagnostics is used in SwissFEL to measure beam properties and to stabilize the beam parameters through feedback.

Separate measurements of the two bunches can be performed in dedicated beam times by simply turning off one of the photocathode lasers. This method, however, neglects any effects that the presence of the first bunch could have on the second (e.g., beam loading of the rf structures and so on), and it is not convenient to be used in routine operation. For these reasons, and to enable beam-based feedback, diagnostics for the key beam parameters capable of distinguishing the two bunches has been developed. This includes both transverse and longitudinal diagnostics, as outlined in the following sections.

A. Beam position monitors

The transverse position of the electron bunches in SwissFEL is measured by 178 cavity beam position monitors (CBPMs), each having two rf resonators. The so-called reference resonator is used to measure the bunch charge through its TM_{010} mode. The TM_{110} mode of the "position" resonator produces a signal mainly proportional to the product of beam position and charge and in this way provides information on the transverse beam offset. Frequency-dependent drift effects in the electronics are minimized by choosing the same operating frequency and loaded quality factor Q_L for both resonators. To eliminate the charge dependency, the transverse beam position is obtained by normalizing the position resonator signal to the reference resonator signal amplitude. The signals' ratio is converted into millimeters beam offset using a suitable scaling factor.

In the undulator area, two CBPM types ("high-Q CBPMs") with 5 mm (in Athos) and 8 mm (in Aramis) aperture are used to measure the position of single bunches at 100-Hz repetition rate. Their operating frequency and Q-factor are, respectively, 4.9 GHz and 1000. The comparatively high Q_L ensures high position resolution, enabling precision orbit control in the undulator region that is critical for a stable FEL lasing process. For regions where two bunches with 28-ns spacing are present, "low Q-factor CBPMs" are used. They have Q_L of 40, an operating frequency of 3.3 GHz and a 16-mm beam aperture. A longer version with a 38-mm aperture also exists and is used where required. Table II summarizes the CBPM types and their basic parameters.

The low-Q CBPMs are well suited to resolve the individual position and the charge of the two closely spaced bunches because when the second bunch arrives 28 ns later, the signal from the first bunch has already decayed to 0.07% (−63 dB) of its original amplitude. The larger bandwidth of the low-Q CBPMs results in a lower position resolution compared to the high-Q undulator CBPMs. Stainless steel 316LN was chosen for the case material of the low-Q CBPMs, while the high-Q ones have a copper-steel hybrid design to ensure better conductivity of the inner (copper) surface. This construction ensures a high Q-factor with a mechanically robust outer case and flanges made of stainless steel. To achieve the desired sub-micron position resolution over the full bunch charge range (10–200 pC), the geometry of all CBPM resonators was optimized for signal strength. For signal extraction, the position resonators use waveguide couplers to suppress the undesired TM_{010} mode that may otherwise limit the CBPM performance. In the reference resonators, one (in the CBPM with 16-mm aperture) or two (in the CBPM with 38-mm aperture) inductive couplers are used directly in the resonator (Fig. 7, right-hand side connectors) to pickup the signal.

TABLE II. SwissFEL CBPM types.

	CBPM38	CBPM16	CBPM8	CBPM5
Aperture	38 mm	16 mm	8 mm	5 mm
Quantity	6	116	34	22
Length	255 mm	100 mm	100 mm	100 mm
Bunches	1–3		1	
Bunch spacing	28 ns		10 ms	
Frequency	3.28 GHz		4.93 GHz	
Q_L	40		1000	
Usage	Linac/transfer		Undulators	

The low-Q resonator CBPM signal is IQ mixed with a 3.3-GHz local oscillator rf signal to be directly down-converted to baseband. The high-Q resonator CBPM signal is first converted to an intermediate frequency of 136 MHz and then digitally downconverted to baseband. Both CBPM types have 16-bit 160 Ms/s differential Analog-to-Digital Converters (ADCs), excluding Athos undulator CBPMs, where a newer 16-bit 500 Ms/s ADCs are used. All CBPM electronics was developed in-house.

The bandwidth of the low-Q CBPM electronics was chosen as an engineering compromise between low cross-talk from the first bunch to the second (requiring larger bandwidth) and low noise (achieved with smaller bandwidth), still reaching submicron position resolution down to 10 pC bunch charge and 0.07% relative charge resolution, limited by its absolute limit of ∼5 fC at low bunch charge [22]. A simplified block diagram of the low-Q CBPM electronics is shown in Fig. 8.

Presently, no crosstalk removal algorithms are used. Typically ∼1% of the signal amplitude of the first bunch overlaps with the peak signal of the second bunch and,

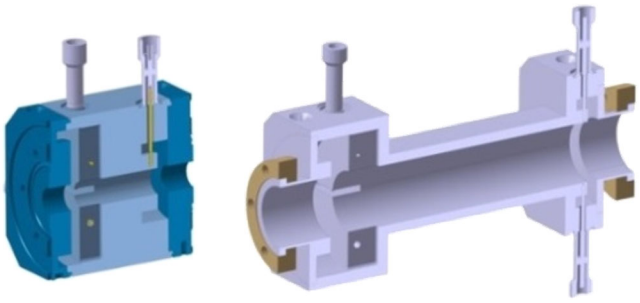

FIG. 7. 3D model cross-section view of the SwissFEL CBPM16 (left) and CBPM38 (right).

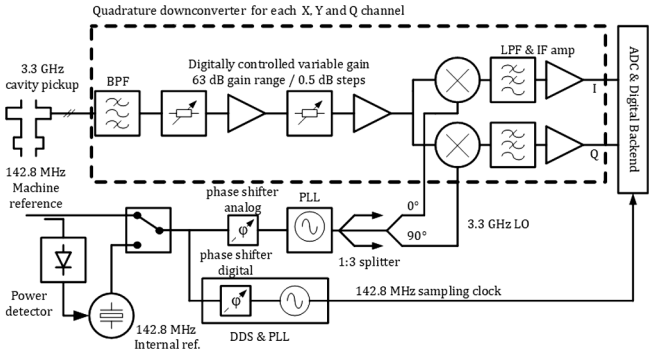

FIG. 8. Simplified block diagram of low-Q CBPM rf front-end electronics, showing only one of its three input channels (one reference and two position signal channels).

respectively, affects its charge measurement. This crosstalk is predominantly caused by the band-pass and low-pass filters in the CBPM electronics. The crosstalk was measured by comparing the measured charge value of a CBPM upstream of the switchyard (seeing both bunches) with the one from a CBPM downstream of it (seeing only the second bunch), while switching on and off the first bunch and observing the measured charge values of the second bunch. Due to a symmetric electronics design of "position" and "charge" channels, the position crosstalk is expected to be <2% of the beam offset. The systematic error (due to crosstalk) in the second bunch position measurement could be further reduced by centering the first bunch in the CBPM since the position crosstalk is in first order proportional to the beam offset from the CBPM center. For a beam offset of ∼100 μm, the resulting systematic second bunch position measurement error is <2 μm. Presently, bunch charge and repetition rates in Aramis and Athos are usually equal and the bunch-to-bunch crosstalk is rather reproducible, making it of minor relevance for machine stability and operation. For future operation modes with more flexible charge ratios and bunch repetition rates, we plan to digitally suppress the crosstalk. One way to achieve this is to use the amplitude and phase at the peak of the first bunch signal and extrapolate it to the time of the second one. Using digital processing, the extrapolated signal can be subtracted from the superimposed signals of both bunches after the passage of the second bunch, leaving only the signal of the second bunch.

Table III summarizes the measurement limits of the different CBPM types.

TABLE III. Measured CBPM charge limits and position noise.

	CBPM38 CBPM16	CBPM8 CBPM5
Charge range	10–400 pC	
Relative charge resolution	<0.07%	<0.04%
Absolute charge resolution	<5 fC	<1.5 fC
Position noise @ 10–200 pC	<1 μm	<0.5 μm
Position noise @ 1 pC	<8 μm	<5 μm

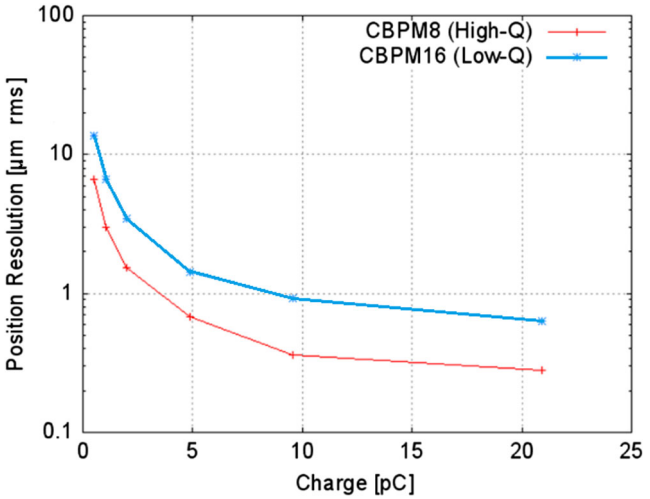

FIG. 9. Absolute single-bunch position resolution as a function of the bunch charge.

The CBPMs are used not only to control and correct the beam orbit, or for beam-based position alignment measurements, but also for other purposes, such as beam energy or beam loss measurement. The beam energy is determined by CBPMs in dispersive sections like beam dumps, or the arms of the bunch compressors, where a dispersion in the order of 0.1 m results in a relative beam energy resolution of $\sim 1 \times 10^{-5}$. Since the CBPMs are presently used by electron beam energy feedback, their stability has a direct impact on the x-ray beam energy stability.

The charge resolution and bunch-to-bunch crosstalk of the CBPMs are about an order of magnitude better than the dedicated charge monitors ("Turbo-ICT2", described in the next section) installed at various locations in SwissFEL. Therefore, the CBPM measurements are also used by individual bunch-charge feedbacks for both bunches. Figure 9 shows the absolute single-bunch position resolution as a function of bunch charge for the high-Q and low-Q CBPMs.

After production, the position and charge sensitivity of each CBPM were measured in the lab, and all CBPM electronic modules were calibrated using a signal generator that simulated the beam signal. In addition, beam-based calibrations using other dedicated charge monitors were and are done regularly to cross-check and recalibrate the absolute charge scaling factors of the CBPMs.

B. Beam charge monitors

The charge monitors were designed with the requirements to discriminate 28-ns dual-bunch structure and to cover the charge range from 10 to 200 pC with a sensitivity of a few pC. To fulfill such demands, SwissFEL is equipped with several integrating current transformers of the type Turbo-ICT2 by Bergoz [23–25]. The Turbo-ICT2 can resolve each bunch separately thanks to a suitable reduction

of the quality factor of the current transformer resonance of a standard Turbo-ICT. A total of six Turbo-ICT2 are installed in SwissFEL. They can monitor the individual charge of the two bunches at the gun, after the first compression stages as well as the single bunch charge in the Aramis and Athos beamlines after bunch separation. Most recently, the Turbo-ICT2 readings were validated and corrected by comparison with other monitors, including reference resonator signals of CBPMs. The CBPM signals were directly sampled with a fast oscilloscope, and the charge was determined by fitting the expected resonator signal to the oscilloscope waveform, applying a suitable scaling factor obtained by accurate calibration of the involved rf components [26].

An additional charge measurement in the gun section of SwissFEL is provided by a wall current monitor. This monitor is used for the individual bunch charge readout, in particular, to determine a coarse timing overlap (∼100 ps) between the rf gun phase and the arrival time of the laser onto the cathode.

C. Bunch arrival-time monitors

The SwissFEL bunch arrival-time monitors (BAMs) [27] are nondestructive longitudinal diagnostic systems, with drift, stability, and resolution in the femtosecond range. They are based on Mach-Zehnder intensity modulators, which encode the bunch arrival time in the amplitude of a mode-locked laser pulse [28]. They derive their <10-fs drift stability through length-stabilized single-mode fiber optical links [29].

An in-house developed 12-bit Generic PSI ADC Carrier (GPAC) ADC [27], samples the laser pulses at 285.6 Ms/s, which is twice their repetition rate. Thus, always one peak and one baseline point are sampled (Fig. 10).

The ADC clock is derived directly from the same optical laser pulses and is thus synchronous with them. Amplitude measurement of multiple reference laser pulses preceding the interaction with the first bunch allows *in situ* determination of the laser amplitude jitter and thus the instantaneous BAM resolution. The latter depends on the bunch charge and varies between 6 and 1 fs rms for 10 and 200 pC, respectively. The arrival time is encoded in the amplitude of one of the reference laser pulses, modulated

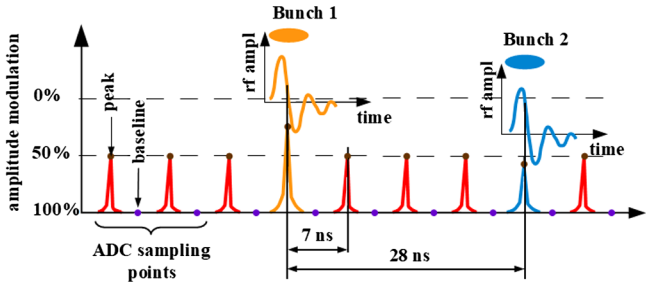

FIG. 10. ADC sampling principle of the SwissFEL BAM.

by the electrical rf transient generated by a large bandwidth button pickup close to its zero crossing [30,31]. Each of the two bunches is measured by an ADC sample separated by eight sampling periods (28 ns) as it is depicted in Fig. 10. To ensure acquisition close to the zero-crossing of the pickup rf transient, each BAM has a linear, servo motor driven, optical delay stage used for zero-crossing feedback [31]. The arrival time is the combination of the readout of the ADC and the position of the delay stage. In the presence of two bunches simultaneously, the zero-crossing feedback runs on the first bunch. If there is only one bunch in the machine, the zero-crossing feedback runs on that particular bunch regardless of its position (bunch one or bunch two). To secure bunch synchronous acquisition, both the ADC and the motor encoder readouts are triggered with dedicated timing events. In the present implementation, the BAM server runs on a Versa Module Europa (VME)-based input/output controller (IOC) and an external VME-based event receiver EVR-300. The physical triggers for the ADC and the motor encoder are a logical OR function of the two bunches' timing events. Because the ADC has only one trigger input and it is triggered by the combined signal of the two bunches' events, it is not possible for the IOC to filter out the information for the lower repetition rate bunch (usually the second bunch). Thus, presently, the measurement for the lower repetition rate bunch has "gaps." To overcome this, we are currently working on the implementation of an embedded event receiver with programmable trigger lines, running on a power PC on the GPAC ADC carrier board.

This will allow for the independent triggering of channels belonging to the first bunch or to the second one. Additionally, there will be a mask allowing the IOC to discriminate between the two bunches independently on their repetition rate. In the shown example, the zero-crossing feedback runs on the first bunch. The arrival-time jitter calculated as a moving standard deviation over 1 s (100 bunches) is 13 fs. Figure 11 illustrates the bunch arrival-time measurement for the two bunches at 100 Hz, at a BAM located downstream of the laser heater system. Due to the small time separation between the two bunches, there is a principal difficulty to measure the second bunch accurately when the first one is present in the machine. The wakefield created by the first bunch can be picked up by the large bandwidth button pickup (40 GHz) leading to an undesired additional modulation (crosstalk). The typical value of the crosstalk is 20% modulation (transferred from the first bunch to the second) which results in about 120-fs absolute timing shift of the second bunch. The large pickup bandwidth and the small beam chamber diameter are crucial for the BAM resolution, therefore, it is not possible to completely avoid this disturbance. Only the two BAMs located upstream of the switchyard (at the laser heater and at the Linac 1) are affected by this problem.

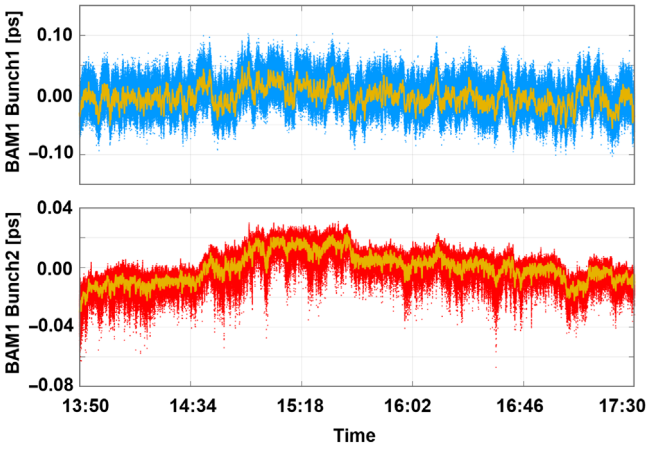

FIG. 11. First bunch (upper plot) and second bunch (lower plot) arrival times at 100 Hz repetition rate measured by the BAM at the laser heater, downstream of the photocathode gun at $Z = 13$ m.

D. Bunch compression monitor

In SwissFEL, the two bunches are longitudinally compressed from a few picoseconds down to a few femtoseconds rms. This is done in two magnetic chicanes using the energy chirp from off-crest acceleration in the rf structures of the injector and of the linac. The bunch compression is monitored by the so-called bunch compressor monitors (BCMs) [32]. The design specifications of the SwissFEL BCMs are full noninvasiveness; 100-Hz online monitoring of each of two bunches; signal integration into the machine feedback to stabilize the compression; signal detection covering the full charge range from 10 to 200 pC, as well as robust and fully automatized functionality during machine operations. To fulfill these requirements, the operation principle of the SwissFEL BCMs is based on the nondestructive detection of the temporal coherent threshold of synchrotron and diffraction radiation emitted by the electron bunch. The signal readout is the result of the time integration of the radiation intensity over the whole acceptance wavelength band of the detectors. Hence, no frequency discrimination of the spectral distribution of the detected radiation is applied. Consequently, the monitor readout is simply a bunch-length dependent and uncalibrated signal. The monitoring of the bunch length at the first compression stage (rms bunch length of a few hundred fs) is ensured by a BCM detecting the coherent synchrotron radiation emitted by the electron beam at the entrance of the fourth dipole of the first magnetic chicane. The monitor is equipped with two broadband Schottky diodes (0.3–2.0 THz), which are able to discriminate at 100 Hz the dual bunch structure of the electron beam.

After the second magnetic chicane, the bunch length monitoring at the final compression stage is ensured by a BCM that detects the coherent threshold of the diffraction radiation emitted by the electron bunch when crossing a metallic screen with a slit. The monitor is equipped with a fast mercury cadmium telluride detector, which is also capable of discriminating the dual-bunch structure of the beam.

The signal readout of the two BCMs in operation at the two compression stages is integrated into the machine feedback to stabilize the compression. A further BCM is installed after the energy collimator of the Aramis undulator line. It is used for a final compression monitoring of the single bunch under particular machine setting conditions (10 pC and bunch duration below 3-fs rms).

E. Synchrotron radiation monitor

Synchrotron radiation monitors (SRMs) are installed in the chicanes of the bunch compressors. Imaging the incoherent radiation from the third dipole, located in the dispersive section, SRMs can measure the energy and the projected energy spread of the beam [33].

After an upgrade, the SRM in the first bunch compressor can measure each bunch individually up to the maximum machine repetition rate. A microchannel plate is activated only for a few nanoseconds to select the first or the second bunch. The output of the microchannel plate is then imaged onto a CMOS image sensor.

VI. SWITCHYARD

The SwissFEL beam switchyard consists of two fast high Q-factor resonant deflecting magnets: kickers (K1 and K2), three compensating dc dipole magnets (D1, D2, and D3), and a Lambertson dc septum (S). Between the resonant kickers (RKs) and the septum, there are four quadrupole magnets (Q1–Q4).

Figure 12 schematically shows the trajectory of the beam in the switchyard region.

The bunches arrive synchronized with the positive and negative crests of the RKs' sinusoidal magnetic field and

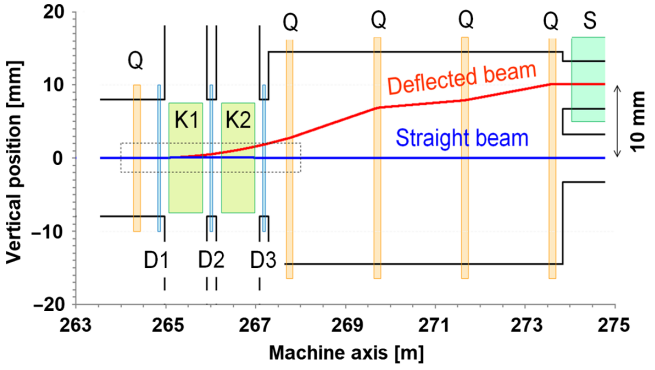

FIG. 12. Beam trajectory in the switchyard with the corresponding deflecting field regions. Q denotes quadrupole magnets, K1, K2-resonant kickers, D1, D2, and D3-compensating dipole magnets, and S-the septum.

are deflected up and down, thus separated vertically. The compensating dipole magnets equally act on both bunches, deflecting them upwards. The amplitude of the RKs and the compensating dipole magnets is automatically set to provide trajectory compensation for the down-kicked bunch and the required deflection for the up-kicked bunch according to the beam energy. The total resultant deflection angle (from the RKs, compensating dipole magnets and the quadrupole magnets) is about 1 mrad. Some 10 m further downstream, the up-kicked bunch enters the septum 10 mm above the beam axis, to be finally deflected toward the Athos beamline. The down-deflected bunch returns to its original trajectory and enters the zero-field septum region (8.2 mm diameter hole) to continue straight on the Aramis axis. If the phase of the RKs is inverted, the first bunch is deflected down (and continues straight to Aramis) while the second is deflected up and enters the transfer line toward Athos. If the RKs are off (put on delay), there is no bunch separation and depending on the compensating dipole magnets' settings, both bunches are directed either to Aramis or to Athos. This covers all possible separation scenarios.

The RKs are operated at 100 Hz to ensure the simultaneous serving of the two experimental beamlines up to the maximum machine repetition rate. To maintain their thermal operating point, they are continuously running even if the separation is not needed.

The desired machine operation mode is set by a high-level timing/bunch mapping control panel that coordinates all relevant systems.

To make the separation fully transparent (no FEL disturbance), the required overall switchyard relative stability was determined to be $\pm 10 \times 10^{-6}$ pk-pk. Equipartitioning the error budget among the components and inverse scaling it with the deflection angle, we require the total kickers' relative stability to be better than $\pm 160 \times 10^{-6}$ pk-pk. Again equally distributed over the two kickers, we need $\pm 80 \times 10^{-6}$ pk-pk for each kicker ($\pm 40 \times 10^{-6}$ for pure amplitude jitter and ± 110 ps time jitter for phase-driven amplitude instability or another $\pm 40 \times 10^{-6}$). This is a conservative approach assuming the worst-case scenario where all instabilities are correlated and add up linearly (including the amplitude- and the phase-driven instabilities).

For the septum, the relative amplitude stability requirement was set to $\pm 5 \times 10^{-6}$ pk-pk [3].

Two RKs are used, one after the other, to provide up to $\sim$2 mrad separation angle between the two bunches. Taking into account the effect of the quadrupole magnets between the RKs and the septum, it results in a 10-mm vertical bunch separation at the septum entrance. The Lambertson septum deflection angle is 33 mrad in the perpendicular (horizontal) plane. For this reason, the beam in Athos dogleg is 10 mm higher and needs vertical correction to be brought back to the proper beam height.

TABLE IV. Resonant kicker parameters.

Parameter	Given	Derived
Particle energy	3.3 GeV	
Magnetic length	770 mm	
Separation angle	0.5 mrad	
Bunch separation	28 ns	
Frequency	17.85 MHz	
Magnetic field		$\pm$3.6 mT
Number of turns	1 turn	
Inductor bars diameter	20 mm	
Vertical aperture	15 mm	
Current amplitude		162 A
Voltage amplitude		7.2 kV
Resonator inductance		397 nH
Resonator capacitance		200 pF
Loaded Q-factor		480

A. Resonant kickers

Electrically, the RKs are lumped partially-driven LC resonators. When the resonator is excited, its alternating current produces an alternating deflecting magnetic field. To separate the two bunches, the resonance frequency of the LC circuit is tuned to have a period equal to twice the bunch time separation. The resonant current is synchronized such that the bunches arrive at the positive and the negative maxima of the sinusoidal current (i.e., magnetic field). This reduces the required "separation" current by a factor of 2.

Table IV summarizes the parameters of the RKs.

1. Construction

Figure 13 shows the interior of the RK. Due to the required relatively high operation frequency (17.85 MHz), no ferromagnetic core is used. Two 20-mm diameter copper bars, parallel to the beam (top and bottom), form the resonator's inductor. They are supported by transverse ceramic plates that isolate the bars electrically and provide a thermal path for the dissipated heat. The two sides of the base plate are water-cooled by a high-precision (± 0.1 °C) water circuit to keep the resonator temperature constant.

At one end of the bars, there are two high voltage (HV) vacuum capacitors, which form the resonator's capacitor. Two copper side vanes are used to tune the resonator frequency. One is for rough manual tuning, while the other is motorized and allows for remote tuning. Operating on the crest of the resonance curve ensures minimum sensitivity to driver phase noise and is crucial for the stability performance of the system [34]. Due to the partial driving of the resonator, the HV (over the resonator capacitors) is restricted inside the vacuum chamber thus smaller excitation voltages are required. This relaxes the voltage requirements for the vacuum feedthroughs, the connecting coaxial cables, and the driver.

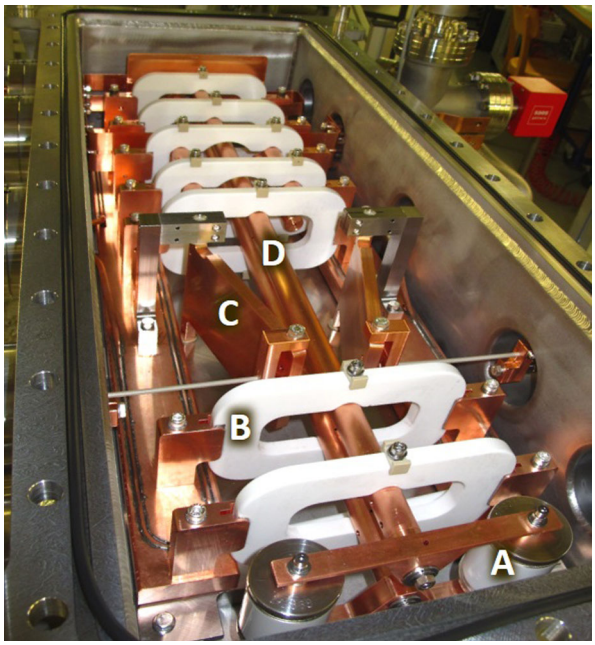

FIG. 13. Resonant kicker in the vacuum tank: A—vacuum capacitor (resonator capacitor), B—ceramic plate, C—tuning vane, and D—copper bar (resonator inductor).

2. Synchronization

In this novel approach, the kickers' deflection is a sine wave. This makes the proper timing of the devices crucial for their correct operation. The RKs are high Q-factor resonators, which need time to reach steady-state resonance amplitude before they are ready to deflect the electron bunches. The synchronization block receives a trigger signal of about 100 μs before the beam arrival time from the conventional accelerator timing system and resynchronizes it with a high-stability rf reference signal. An ECL logic provides the necessary low-jitter signals to the rest of the system. The synchronization block monitors the pulsed parameters programmed by the operator (such as pulse duration and repetition rate) and gives a warning or blocks RKs operation if any limits are exceeded.

3. Driver

To ensure resonance excitation, a high amplitude-stability and low phase-noise solid-state rf driver was developed. It provides up to ∼7 kW of rf power during the excitation period. The output MOS FET power stages are supplied by a high-precision, programmable voltage regulator with 1×10^{-6} resolution. Each driver has four rf power modules and each of them has a separate coaxial output. Four low-loss coaxial cables deliver the rf power to the kicker. A four-way Wilkinson power combiner adds the rf power that excites the RK resonator. The driver is temperature stabilized by a high-precision (±0.1 °C) water circuit.

4. Full-range measurement system

The full-range measurement system provides amplitude and phase information about the oscillating current of the kickers. It is based on fast (250 MHz), high-resolution (16-bit) ADCs interfaced by an field-programmable gate array logic (Virtex 6, Xilinx). Digital synchronous detection and signal processing is used to obtain the amplitude and the phase information with high resolution. It was found that the signal-to-noise ratio is basically limited by the $1/f$ performance of the ADC chips, and even with extensive averaging of two ADCs working in parallel, the measurement amplitude precision is limited down to about 1×10^{-5} rms [35].

5. Precision measurement system

For higher-performance measurements, a complementary offset-based precision-measurement system was designed and built [36,37]. A high-stability programmable dc offset with 1×10^{-6} resolution is subtracted from the measured sine-wave signal and the difference is amplified and measured. In this way, at the expense of measurement dynamic range reduction, higher measurement resolution and lower noise floor could be achieved. The system is temperature stabilized by a high-precision (±0.1 °C) water circuit. Using statistical analysis, the relative noise floor of the built precision measurement system is evaluated to be $\sim 8 \times 10^{-7}$ rms [32].

6. Electrical stability

The pulse-to-pulse amplitude jitter of the RKs during routine operation is $2–3 \times 10^{-6}$ and the phase stability is 2 to 3 millidegree averaged over the rf macro pulse. An amplitude feedback (using the precision measurement system) and a phase feedback (using the full range measurement system) control the amplitude and phase of the RKs with high precision.

B. Lambertson septum magnet

For the magnet technology of the septum, there was a choice between pulsed eddy current and dc Lambertson septa. For the SwissFEL application, the 100-Hz repetition rate gave rise to uncertainties associated with the effect of mechanical "hammering" that would occur with a pulsed magnet. On the other hand, a Lambertson design has the drawback of requiring two more dipoles in the dogleg section of the beam path to the Athos beamline to remove the 10-mm vertical offset necessary for passage through the dipole gap of the septum magnet. For the sake of better operational stability, the Lambertson design was selected for implementation in SwissFEL. Table V summarizes the septum parameters.

An in-vacuum design was chosen because the 10-mm separation between straight-through and deflected beam left no reserve for thin-walled vacuum pipes (with tolerances in the 0.7 mm range) to pass through the magnet

TABLE V. Lambertson septum parameters.

Parameter	Given	Derived
Particle energy	3.3 GeV	
Magnetic length	760 mm	
Angle	34.9 mrad	
Bending radius		21.8 m
Magnetic field		510 mT
Effective magnet width	80 mm	
Effective magnet gap	9.8 mm	
Number of turns	41 turns	
Inductance near dc		13 mH
Inductance at 1 Hz		1.5 mH
Current		98 A
Conductor cross section	47 mm^2	
Total series resistance		29 mΩ
Voltage		2.68 V
Power loss		247 W

apertures. The magnet is novel because there is a 1-mm thick copper plate separating air from the vacuum with the magnetic flux passing through this plate (Fig. 14).

The 8.2 mm diameter hole in the iron core is for the passage of the straight-through beam. In this region, the leakage field should be as small as possible. The magnetostatic solver of CST Studio Suite® was used to explore options to minimize the leakage field, for example, by stacking thin sheets of electrical sheet and mu metal. Figure 15 shows the magnetostatic model of the septum. However, the effect of practical micrometer-scale gaps with stacked sheets gave poorly controlled leakage fields.

A production technique of deep hole boring or "cannon boring" could give exceptionally straight holes with finely polished surfaces at a low cost. The 760-mm long magnet iron core was carefully machined with various flat surfaces

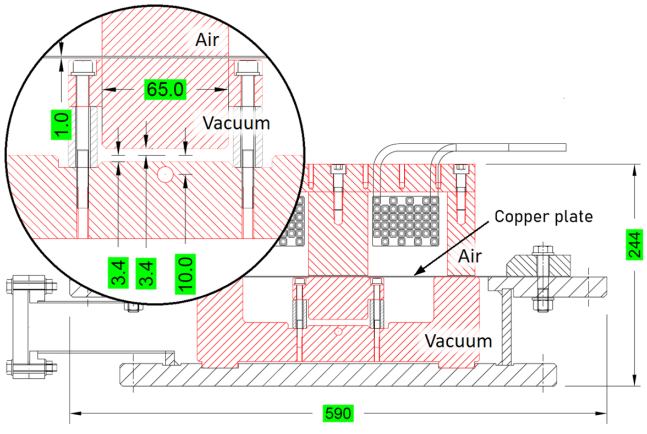

FIG. 14. Cross section of the septum magnet, with enlargement of the gap region. The upper half of the iron core with the coil winding is in air, and the lower half with beam apertures is in vacuum, with a 1-mm copper sheet as vacuum sealing. The aluminum support block for the thin copper sealing plate is not shown.

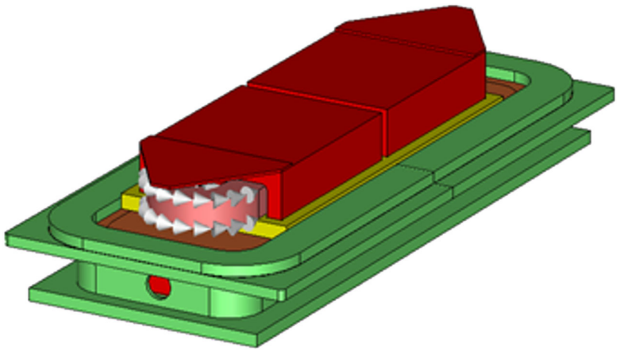

FIG. 15. 3D magnetostatic model of the septum. Additional triangular plates bolted on the magnet at each end add a negative stray field to reduce the total leakage field integral to <50 μTm.

for precision alignment inside the vacuum chamber, and with an 8.2-mm hole for the beam passage, leaving 2.5 mm of iron as effective septum thickness.

In Fig. 16, we show leakage field measurements performed with a Lake Shore Cryotronics Gaussmeter Model 460-10, together with two modified MMZ-2536-UH-06 3D probes and a custom measuring machine.

The effects of depth, diameter, and transverse position of the hole were investigated using simulations. The outcome was that the leakage field is largely what is expected from the permeability of the surrounding iron. If the iron is carrying a flux density of, say, 500 mT with a relative permeability of 5000, then the leakage field would be around 100 μT. The hole geometry is not a predominant factor. The transmission of low-level power supply noise in the range of 10 mHz–10 kHz was both simulated and measured. The bulk iron core gave a strong suppression of noise for frequencies higher than 1 Hz and a corresponding drop of inductance toward zero. The presence of very low levels of 50-Hz noise in the magnet gap was due to stray

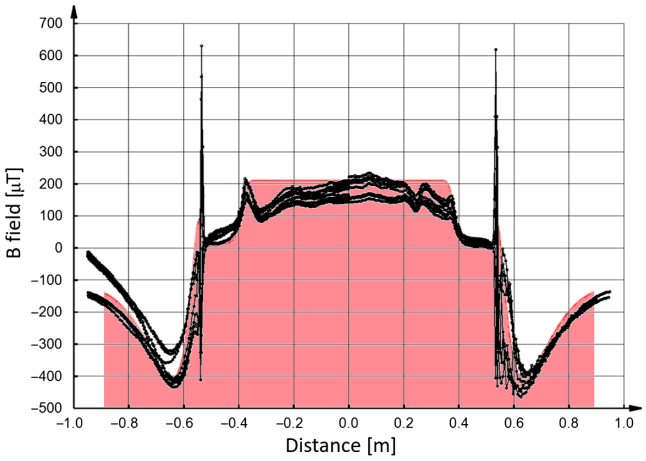

FIG. 16. Simulation (colored area) and measurement (lines) of the septum leakage field. The measurement curves show several runs overlaid, with differences mainly due to hysteresis from varying magnet cycling.

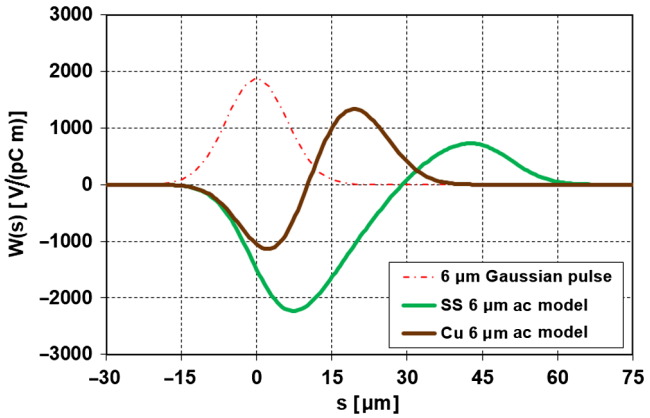

FIG. 17. Longitudinal wakefields for the 8.2-mm diameter hole for stainless steel and copper and the corresponding Gaussian test pulse. The lower loss with copper gave the incentive to add copper plating.

magnetic fields in the laboratory rather than the power supply itself.

The deflection field homogeneity was simulated but efforts to improve the homogeneity on the part-per-thousand level were subject to simulation meshing errors. The easier solution was to make the pole tip wider, without shimming. The pole tip is ~65 mm wide, with a gap of 6.8 mm.

For bunches longer than 50 μm, the effect of resistive wakefields could be well modeled with CST using local meshing. In this range, the results agree well with the analytical solutions. Below 10 μm bunch length, an analytical solution was used, and the results for stainless steel and copper are shown in Fig. 17. Based on this result, it was decided to copper-coat the zero-field septum channel.

C. Separation stability

Due to the effects arising from the RKs, the bunch-separation system is expected to be the most critical element concerning electron beam stability. Since both bunches are deflected, it is possible to check the stability using the bunch going straight through to the Aramis beamline (in single bunch mode). A direct comparison between the bunch going straight through (all deflecting elements off) and when it is deflected (down) and back-compensated to go on axis was done for electron beam trajectory, electron beam shot-to-shot position stability, FEL photon beam shot-to-shot pulse energy and pointing stability. No significant changes in the horizontal and vertical beam trajectories were found [38], thus validating the amplitude ratio between RKs and compensating dipole magnets.

1. Electron beam stability

Figure 18 shows shot-to-shot horizontal and vertical electron beam position running standard deviations of 100 consecutive pulses measured by a CBPM right before the

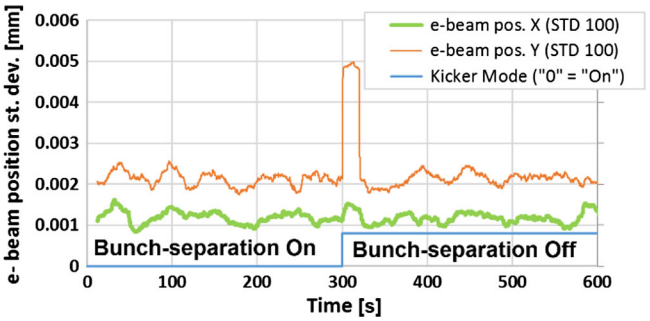

FIG. 18. Electron beam position running standard deviation of 100 consecutive pulses right before the FEL undulator section with the bunch-separation system on and off.

FEL undulator section. Note that the bunch-separation system is on when the "Kicker mode" signal is zero (bottom curve in Figs. 18–20).

The large jump of the vertical standard deviation at around 300 s is due to the turn-off transient of the deflecting elements. The reprogramming of the RKs and the compensating dipole magnets is not beam synchronous and could lead to vertical beam disturbance for a short period of time. No noticeable change in electron beam stability is observed with and without bunch separation.

2. FEL photon beam stability

The effect of the bunch-separation system on the FEL photon beam pulse-to-pulse stability was investigated as well. Measuring the FEL pulse stability should be an even more sensitive way to detect an electron beam disturbance and in any case represents the ultimate test to determine if the system stability is sufficient.

FEL photon pulse energy stability.—To characterize the FEL photon pulse energy shot-to-shot stability two measurement methods were applied. The first one is based on a nondestructive gas-based pulse-energy monitor [39] while the second is based on an integration of the beam image on a photon beam screen (destructive to the photon beam). Since the camera pixel intensity is proportional to the number of absorbed photons (at an FEL wavelength of 0.5 nm, within the linearity of the screen conversion) the image intensity integral is proportional to the total absorbed photon pulse energy (not to the x-ray pulse electromagnetic field intensity). Figure 19 shows the running average of 100 consecutive pulses of the gas-based pulse-energy monitor. It can be seen that FEL pulse energy does not depend on the presence of bunch separation. The running standard deviation of the two measurements (gas-based and screen-based) is shown there as well. Reprogramming of the switchyard elements is not beam synchronous so to avoid beam losses during switching from "bunch-separation on" to "bunch-separation off" the electron beam is shortly blocked. During this time the running standard deviation of the two measurements is not

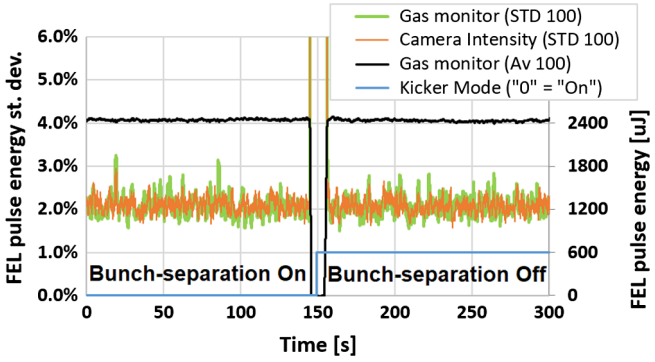

FIG. 19. FEL photon beam pulse energy (running average of 100 consecutive pulses) measured by the gas-based monitor and its running standard deviation of 100 consecutive pulses measured with gas-based monitor and photon beam image camera with the bunch-separation system on and off.

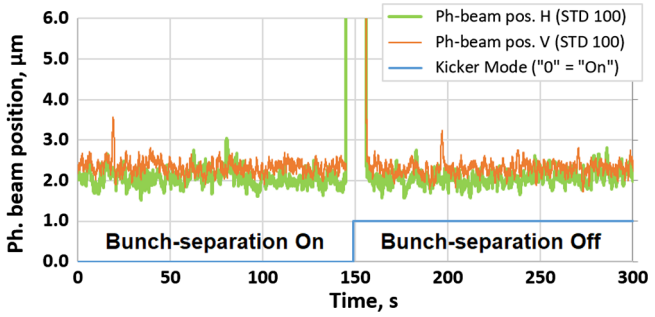

FIG. 20. FEL photon beam horizontal and vertical position standard deviation of 100 consecutive pulses with the bunch-separation system on and off.

valid and has large jumps. Again, the data show no effect on beam stability due to the bunch-separation system.

FEL pointing stability.—The effect of the bunch-separation system on the FEL beam pointing was also investigated using the same beam image camera described above. Figure 20 shows the horizontal and vertical position running standard deviation of the beam center of mass for 100 consecutive pulses.

The large jumps in the middle are due to turning off the electron beam (like in the previous figure), respectively, no valid beam position data exist during this period. There is no notable change in the FEL pointing stability due to the bunch-separation system.

VII. OPERATIONAL AND USER LIMITATIONS

For the double bunch operation, we use two fully independent laser systems to generate the two bunches at all available repetition rates. The mapping of laser-to-bunch and bunch-to-beamline relation can be changed easily. Also, both bunches can be sent together into either beamline. The individual bunch control is not only convenient for bunch length measurements or special beam operation modes but also to react to system failures. For example, when there is an rf failure just in the Aramis part, the Athos branch continues to operate undisturbed. However, running the second bunch at a higher repetition rate than the first bunch may cause instabilities and hiccups in the feedback systems. Therefore, in standard operation, the orbit feedbacks only act on the first bunch (but this could be configured differently).

Thanks to the accelerating structures downstream of the switchyard (Linac 3 for Aramis and one C-band station in the Athos branch) both beamlines benefit from independent electron beam energy tuning. The electron beam energy can be varied from 2.2 to 6.2 GeV in Aramis and from 2.98 to 3.33 GeV in Athos. In addition, the variable gap undulators offer an extratuning range for the photon energy without changing the electron beam energy. The photon wavelength range achieved in beam operation so far is 0.08–0.51 nm for Aramis and 0.77–4.96 nm for Athos. Both methods for scaling the photon beam energies are used in operation and, thanks to highly automatized rf and optics high-level controls, can be used directly by the end stations. The double bunch operation comes, however, with some limitations in the tuning range of the two FEL lines due to the fact that the two bunches are experiencing the same focusing and accelerating fields upstream of the switchyard. The independent tuning range of the second bunch is restricted to the gun laser settings (delay, pulse energy, position, and profile) and to the limited tuning range offered by the step function applied to the LLRF system described above. This tuning step is sufficient to provide independent energy and compression controls for the feedback in the bunch compressors but the limited step size is not sufficient for significant differences in electron bunch length, charge, and photon pulse bandwidth between the two beamlines. The photon pulse duration can be controlled independently in both beamlines by using wakefields in the dechirper structures to suppress lasing in the head and tail of the bunch, effectively shortening the photon pulse, albeit at the expense of photon pulse energy.

VIII. CONCLUSION AND OUTLOOK

The double bunch operation allows simultaneous operation at the full machine repetition rate (100 Hz) in the two SwissFEL beamlines: Aramis and Athos. The machine now routinely operates in this mode and the scheme has demonstrated excellent reliability and stability. The separation of the two closely (28 ns) spaced electron bunches does not degrade the FEL performance. The photon wavelength range achieved so far is 0.08–0.51 nm and 0.77–4.96 nm in Aramis and Athos, respectively.

Nevertheless, the double bunch operation also introduces some limitations in the setup of the two beamlines, mainly due to the limited independent tuning range of the acceleration parameters of the two bunches in the common part of the machine.

Following the success of the SwissFEL double bunch operation, we are looking at possibilities to further increase the facility's efficiency by extending the scheme to three or even four bunches. Preliminary studies indicate that despite considerable challenges, such an extension may indeed be feasible.

ACKNOWLEDGMENTS

The authors would like to sincerely thank all PSI groups that contributed to the realization of this project. Without this collective effort, the success of the SwissFEL double bunch operation would not have been possible.

[1] E. Prat *et al.*, A compact and cost-effective hard X-ray free-electron laser driven by a high-brightness and low-energy electron beam, Nat. Photonics **14**, 748 (2020).

[2] C. J. Milne *et al.*, SwissFEL: The Swiss X-ray Free Electron Laser, Appl. Sci. **7**, 720 (2017).

[3] R. Ganter, SwissFEL Conceptual Design Report, version 10–04, Paul Scherrer Institut., Villigen PSI, Switzerland (2012).

[4] R. Abela *et al.*, The SwissFEL soft X-ray FEL beamline: Athos, J. Synchrotron Radiat. **26**, 1073 (2019).

[5] T. Beukers, M. Nguyen, and T. Tang, Discrete element transmission line beam spreader kickers for LCLS-II, in *Proceedings of the 2018 IEEE International Power Modulator and High Voltage Conference, Jackson, WY* (IEEE, New York, 2018), 10.1109/IPMHVC.2018.8936755.

[6] K. Tono, T. Hara, M. Yabashia, and H. Tanaka, Multiple-beamline operation of SACLA, J. Synchrotron Radiat. **26**, 595 (2019).

[7] L. Froehlich *et al.*, Multi-beamline operation at the European XFEL, in *Proceedings of the 39th International Free-Electron Laser Conference, FEL2019, Hamburg, Germany* (JACoW, Geneva, Switzerland, 2019), 10.18429/JACoW-FEL2019-WEP008.

[8] A. Sargsyan, V. Sahakyan, and W. Decking, Parallel operation of SASE1 and SASE3 undulator sections of European XFEL, J. Phys. Conf. Ser. **874**, 012021 (2017).

[9] G. Penco *et al.*, Two-bunch operation with ns temporal separation at the FERMI FEL facility, New J. Phys. **20**, 053047 (2018).

[10] F. Decker *et al.*, Tunable x-ray free electron laser multi-pulses with nanosecond separation, Sci. Rep. **12**, 3253 (2022).

[11] A. Citterio, M. Aiba, and R. Zennaro, Long range wake-fields in the SwissFEL C-band linac, in *Proceedings of the 2nd International Particle Accelerator Conference, San Sebastián, Spain* (EPS-AG, Spain, 2011), pp. 781–783.

[12] M. Pedrozzi and H. Braun, SwissFEL the hard X-ray FEL at PSI: An overview, in *Proceedings of the CLIC Workshop* (CERN, Geneva, Switzerland, 2014).

[13] M. Pedrozzi, M. Calvi, R. Ischebeck, S. Reiche, C. Vicario, B. D. Fell, and N. Thompson, The laser heater system of SwissFEL, in *Proceedings of the 36th International Free-Electron Laser Conference, FEL2014, Basel, Switzerland* (JACoW, Geneva, Switzerland, 2014), paper THP059.

[14] S. Bettoni *et al.*, Overview of SwissFEL dual-photocathode laser capabilities and perspectives for exotic FEL modes, High Power Laser Sci. Eng. **9**, e51 (2021).

[15] A. Vicario, S. Bettoni, A. Lutman, A. Dax, M. Huppert, and A. Trisorio, Two-color x-ray free-electron laser by photocathode laser emittance spoiler, Phys. Rev. Accel. Beams **24**, 060703 (2021).

[16] R. Zennaro, J. Alex, M. Bopp, H. Braun, A. Citterio, H. R. Fitze, M. Pedrozzi, and J.-Y. Raguin, Conceptual design of the C-band module for SwissFEL, in *Proceedings of the 25th International Linear Accelerator Conference, LINAC-2010, Tsukuba, Japan* (KEK, Tsukuba, Japan, 2010).

[17] A. Rezaeizadeh, R. Kalt, T. Schilcher, and R. Smith, An iterative learning control approach for radio frequency pulse compressor amplitude and phase modulation, IEEE Trans. Nucl. Sci. **63**, 842 (2016).

[18] F. J. Decker, K. L. F. Bane, W. Colocho *et al.*, Recent developments and plans for two bunch operation with up to 1 μs separation at LCLS, in *Proceedings of the 38th International Free Electron Laser Conference, FEL2017, Santa Fe, NM* (JACoW, Geneva, Switzerland, 2017).

[19] Z. Geng, Beam-based optimization of SwissFEL low-level RF system, Nucl. Sci. Tech. **29**, 128 (2018).

[20] N. Milas and S. Reiche, Switchyard design: Athos, in *Proceedings of the 34th International Free-Electron Laser Conference, FEL2012, Nara, Japan* (Kyoto University, Kyoto, Japan, 2012).

[21] S. Bettoni *et al.*, Beam manipulation using self-induced fields in the SwissFEL injector, in *Proceedings of the 9th International Particle Accelerator Conference, IPAC-2018, Vancouver, BC, Canada* (JACoW, Geneva, Switzerland, 2018), Vol. 9, pp. 3401–3404, 10.18429/JACoW-IPAC2018-THPAK074.

[22] A. Keil *et al.*, First beam commissioning experience with the SwissFEL Cavity BPM System, in *Proceedings of the 6th International Beam Instrumentation Conference IBIC2017, Grand Rap-ids, MI* (JACoW, Geneva, Switzerland, 2017), pp. 251–254, 10.18429/JACoW-IBIC2017-TUPCF17.

[23] F. Stulle, J. Bergoz, W. P. Leemans, and K. Nakamura, Single pulse sub-picocoulomb charge measured by a turbo-ICT in a laser plasma accelerator, in *Proceedings of the 5th International Beam Instrumentation Conference, IBIC'16, Barcelona, Spain, 2016* (JACoW, Geneva, Switzerland, 2016), pp. 119–122, 10.18429/JACoW-IBIC2016-MOPG35.

[24] F. Stulle and J. F. Bergoz,Turbo-ICT Pico-Coulomb calibration to percent-level accuracy, in *Proceedings of the 38th International Free Electron Laser Conference, FEL2015, Daejeon, Korea* (JACoW, Geneva, Switzerland, 2015), pp. 118–121, 10.18429/JACoW-FEL2015-MOP041.

[25] S. Artinian, J. Bergoz, F. Stulle, P. Pollet, and V. Schlott, Goubau line and beam characterization of TURBO-ICT for SwissFEL, in *Proceedings of the 4th International Particle Accelerator Conference, IPAC-2013, Shanghai, China, 2013* (JACoW, Shanghai, China, 2013), p. 476, paper MOPME005.

[26] G. L. Orlandi, P. Craievich, M. M. Dehler, R. Ischebeck, F. Marcellini, and D. Stäger, Charge measurements in SwissFEL and results of an absolute charge calibration method,

in *Proceedings of the International Beam Instrumentation Conference, IBIC2021, Pohang, Republic of Korea* (JACoW Publishing, Geneva, Switzerland, 2021), paper WEOB01.

[27] V. Arsov *et al.*, First results from the bunch arrival-time monitors at SwissFEL, in *Proceedings of the 7th International Beam Instrumentation Conference, IBIC2018, Shanghai, China* (JACoW, Geneva, Switzerland, 2018), pp. 420–424, 10.18429/JACoW-IBIC2018-WEPA20.

[28] F. Löhl *et al.*, Electron Bunch Timing with Femtosecond Precision in a Superconducting Free-Electron Laser, Phys. Rev. Lett. **104**, 144801 (2010).

[29] J. Kim, J. Cox, J. Chen, and F. Kaertner, Drift-free femtosecond timing synchronization of remote optical and microwave sources, Nat. Photonics **2**, 733 (2008).

[30] A. Angelovski, A. Kuhl, M. Hansli, A. Penirschke, S. M. Schnepp, M. Bousonville, H. Schlarb, M. K. Bock, T. Weiland, and R. Jakoby, High bandwidth pickup design for bunch arrival-time monitors for free-electron laser, Phys. Rev. ST Accel. Beams **15**, 112803 (2012).

[31] V. Arsov *et al.*, Design and commissioning of the bunch arrival-time monitor for SwissFEL, in *Proceedings of the 6th International Beam Instrumentation Conference IBIC2017, Grand rapids MI, 2017* (JACoW, Geneva, Switzerland, 2017), paper TUPCC15, pp. 182–185, 10.18429/JACoW-IBIC2017-TUPCC15.

[32] F. Frei and R. Ischebeck, Electron bunch compression monitors for short bunches-commissioning results from SwissFEL, in *Proceedings of 8th International Beam Instrumentation Conference, IBIC2019, Malmö, Sweden* (JACoW, Geneva, Switzerland, 2019), paper WEPP026.

[33] G. L. Orlandi, R. Xue, H. Brands, F. Frei, Z. Geng, V. Thominet, and S. Bettoni, Bunch length and energy measurements in the bunch compressor of a free-electron laser, Phys. Rev. Accel. Beams **22**, 072803 (2019).

[34] M. Paraliev and C. Gough, Towards sub-ppm shot-to-shot amplitude stability of SwissFEL resonant kicker, in *Proceedings of 2016 IEEE Power Modulator and High Voltage Conference, San Francisco, CA* (IEEE, New York, 2016).

[35] M. Paraliev and C. Gough, Comparison of high resolution balanced and direct conversion measurement of SwissFEL resonant kicker amplitude, in *Proceedings of 2015 IEEE Pulsed Power Conference, Austin, TX* (IEEE, New York, 2015), 10.1109/PPC.2015.7297016.

[36] M. Paraliev and C. Gough, Stability measurements of SwissFEL resonant kicker prototype, in *Proceedings of 2014 IEEE International Power Modulator and High Voltage Conference, Santa Fe, NM* (IEEE, New York, 2014), pp. 322–325, 10.1109/IPMHVC.2014.7287273.

[37] M. Paraliev, and C. Gough, Resonant kicker system with sub-part-per-million amplitude stability, in *Proceedings of the 8th International Particle Accelerator Conference, IPAC2017, Copenhagen, Denmark* (JACoW, Geneva, Switzerland, 2017), paper WEPIK098.

[38] M. Paraliev, S. Dordevic, R. Ganter, C. Gough, N. Hiller, R. Krempaska, and D. Voulot, Commissioning and stability studies of the SwissFEL bunch-separation system, in *Proceedings of the 39th International Free-Electron Laser Conference, FEL2019, Hamburg, Germany* (JACoW, Geneva, Switzerland, 2019), paper WEP038, p. 404.

[39] Juranić *et al.*, SwissFEL Aramis beamline photon diagnostics, J. Synchrotron Radiat. **25**, 1238 (2018).